

Isogeometric Analysis with Proper Orthogonal Decomposition for Elastodynamics

Richen Li¹, Qingbiao Wu^{1,*} and Shengfeng Zhu²

¹ School of Mathematical Sciences, Zhejiang University, Hangzhou 310027, China.

² Department of Data Mathematics & Shanghai Key Laboratory of Pure Mathematics and Mathematical Practice, School of Mathematical Sciences, East China Normal University, Shanghai 200241, China.

Received 22 January 2020; Accepted (in revised version) 21 November 2020

Abstract. We consider reduced order modelling of elastodynamics with proper orthogonal decomposition and isogeometric analysis, a recent novel and promising discretization method for partial differential equations. The generalized- α method for transient problems is used for additional flexibility in controlling high frequency dissipation. We propose a fully discrete scheme for the elastic wave equation with isogeometric analysis for spatial discretization, generalized- α method for time discretization, and proper orthogonal decomposition for model order reduction. Numerical convergence and dispersion are shown in detail to show the feasibility of the method. A variety of numerical examples in both 2D and 3D are provided to show the effectiveness of our method.

AMS subject classifications: 35K20, 65M12, 65M15, 65M60

Key words: Isogeometric analysis, proper orthogonal decomposition, reduced order modelling, elastic wave, generalized- α method.

1 Introduction

Elasticity models are essential in applied mechanics and engineering. The temporal characteristics of elasticity have many applications in elastodynamics, e.g., building structure analysis [1], marine survey [2], geophysics [24, 25] and seismology [18, 26]. Numerical approaches for such problems include finite elements [27, 28], spectral elements [29, 30], mortar elements [31, 32], discontinuous Galerkin method [33, 34], etc. High accuracy can be achieved with large temporal or spatial resolution. The computational costs of discretization methods for such models with time, physical, geometry parameters are high

*Corresponding author. *Email addresses:* richenli@zju.edu.cn (R. Li), qbwu@zju.edu.cn (Q. Wu), sfzhu@math.ecnu.edu.cn (S. Zhu)

when either time step or spatial size is relatively small. Of course, we can reduce the number of degrees of freedom by adaptive methods with locally refining the meshes. However, a posteriori error estimates are not easy to be obtained for complex models with real applications. For real-time simulations and parameter optimization problems, rapid evaluation is essentially required but it is hard to achieve when the number of degrees of freedom of the discretized system is large. In such cases, we therefore resort to reduced order modeling [3].

Proper orthogonal decomposition (POD) is one popular reduced order modeling approach for problems of various interests in engineering such as turbulent flows [4, 39], weather forecasting and optimal control problems (see [3]). POD has been used widely in different fields with different names, e.g. principle component analysis in statistics and Karhunen-Loeve expansion in stochastic analysis. The combination of POD with Galerkin methods for time-dependent partial differential equations (PDEs) [5–7] extract pertinent information of the model system from the high-fidelity instances. The so-called *snapshots* are obtained for the construction of a low-dimensional basis together with the corresponding field information. A low-dimensional system which contains most information of the original system is built through the new basis. The error between the numerical solution from POD-Galerkin method and the exact solution consists of two parts, i.e., the error between snapshot and exact solution and the error between POD solution and snapshot [8, 9]. High-fidelity approximations obtained from a numerical discretization method for PDEs are crucial for obtaining accurate snapshots and POD-Galerkin solutions.

As an emerging method in recent years, Isogeometric analysis (IGA) [13] has been successfully applied to various fields including structural mechanics [12], fluid dynamics [10], acoustics [9, 37], electromagnetism [11], etc. IGA represents a generalization of the isoparametric finite element method and uses NURBS as basis functions, which possess advantages of exact geometry representation, high global regularity (up to C^{p-1} -continuous with p denoting the degree of the piecewise polynomials of the basis), and convenient integration into CAD software using NURBS design workflow. Complex multi-patch domains can be partitioned exactly in IGA. Moreover, efficient h -, p -, k -refinements and hierarchical scheme [40] can be used to increase accuracy and flexibility of numerical solutions.

The motivation of this paper stems from the fact that the accuracy of the reduced order solution obtained with a POD-Galerkin method first requires snapshots' high-fidelity at a reasonable expense of computational efforts. IGA can produce highly accurate numerical solutions for PDEs efficiently. The natural combination of IGA and POD has been successfully applied in parabolic problems [8, 42], convection dominated convection-diffusion-reaction [36], acoustic wave equation [9] and shape optimization problem [41]. The paper continues the previous works [8, 9, 36] and generalizes this model order reduction method for acoustic wave [9] to elastodynamics. We consider numerical dispersion of the method here. Dispersion analysis reveals how accurate the numerical schemes we proposed are with respect to different wave vectors. Dispersion analysis for vibrations

of rods and beams has been performed [35]. Both isotropic and anisotropic elastodynamic problems with IGA have been proposed in [20]. Numerical dispersion in 3D with spectral element method is discussed in [21]. In this paper we focus on the numerical dispersion of IGA-POD method for model order reduction. We solve the embedded IGA-POD-elastodynamic problem and compare numerical errors between the exact solution and POD solution with respect to different wave numbers and directions. A reliable time discretization scheme is necessary here in order to capture sufficient temporal information. High-order methods [22,23] are available in literature. We choose the generalized- α method for the extra control in high-frequency dissipation.

The rest of the paper is organized as follows. In Section 2, we introduce model formulations of the elastodynamic problem, recall the basics of IGA and POD, and derive spatial and temporal discretizations of the model. In Section 3, we analyze numerical dispersion and numerical convergence. In Section 4, numerical examples are presented to show effectiveness and feasibility of our approach. Finally, the conclusion follows.

2 Problem formulation

Let $\Omega \subset \mathbb{R}^d$ ($d=2,3$) be an open bounded domain with Lipschitz continuous boundary $\partial\Omega$. The L^2 inner product and the corresponding norm are denoted by (\cdot, \cdot) and $\|\cdot\|$, respectively. Denote $H^1(\Omega) := \{v \in L^2(\Omega) \mid D_i v \in L^2(\Omega), i=1, \dots, d\}$ with D_i being the partial distributional derivative with respect to x_i . We denote by $(\cdot, \cdot)_k$ the scalar or vectorial H^k inner product and define the corresponding norm $\|v\|_k := \sqrt{(v, v)_k}$ and semi-norm $|\cdot|_k$.

2.1 Spatial discretization

We consider a linear elastic wave equation with a damping factor. Denote by $T > 0$ the final time and by $\rho: \Omega \mapsto \mathbb{R}$ the medium density. Assume that $\partial\Omega = \Gamma_D \cup \Gamma_N$ with $\Gamma_D \cap \Gamma_N = \emptyset$. Let \mathbf{g} and \mathbf{h} be given functions associated with Dirichlet and Neumann boundary conditions, respectively. Let $\mathbf{u}_0(x)$ and $\mathbf{v}_0(x)$ be initial displacement and velocity data, respectively. Denote by \mathbf{f} the function of external force and by ζ the damping factor. We consider:

$$\begin{cases} \rho \frac{\partial^2 \mathbf{u}}{\partial t^2}(t) + 2\rho\zeta \frac{\partial \mathbf{u}}{\partial t}(t) - \nabla \cdot \boldsymbol{\sigma}(\mathbf{u}(t)) + \rho\zeta^2 \mathbf{u}(t) = \mathbf{f}(t) & \text{in } \Omega \times (0, T], \\ \mathbf{u}(t) = \mathbf{g}(t) & \text{on } \Gamma_D \times (0, T], \\ \boldsymbol{\sigma}(\mathbf{u}(t)) \cdot \mathbf{n} = \mathbf{h}(t) & \text{on } \Gamma_N \times (0, T], \\ \mathbf{u}(0) = \mathbf{u}_0 & \text{in } \Omega, \\ \frac{\partial \mathbf{u}}{\partial t}(0) = \mathbf{v}_0 & \text{in } \Omega, \end{cases} \quad (2.1)$$

where $\sigma(\mathbf{u})$ and $\epsilon(\mathbf{u})$ are the stress tensor and strain tensor, respectively with

$$\begin{cases} \sigma(\mathbf{u}) = \lambda \nabla \cdot \mathbf{u} \mathbf{I} + 2\mu \epsilon(\mathbf{u}), \\ \epsilon(\mathbf{u}) = \frac{1}{2} (\nabla \mathbf{u} + \nabla \mathbf{u}^T), \end{cases} \quad (2.2)$$

in which \mathbf{I} is an identity tensor, λ and μ in (2.2) are Lamé coefficients that can be computed from medium's Young's modulus E and Poisson's ratio ν as

$$\lambda = \frac{\nu E}{(1+\nu)(1-2\nu)}, \quad \mu = \frac{E}{2(1+\nu)}.$$

Another two important material parameters of the elastic wave problem, compressional wave velocity c_p and shear wave velocity c_s are defined:

$$c_p = \sqrt{\frac{\lambda + 2\mu}{\rho}}, \quad c_s = \sqrt{\frac{\mu}{\rho}}.$$

Beside Dirichlet and Neumann boundary conditions that will be mentioned below, there are other types of boundary conditions such as symmetric boundary condition and transparent boundary condition [17, 18, 20, 38]. Here we only consider Dirichlet and Neumann boundary conditions for simplicity.

2.1.1 Isogeometric analysis

In this part we recall some basic formulations of B-splines and NURBS [13]. For any α ($1 \leq \alpha \leq d$) and positive integers n_α and p_α , we define the *knot vector* $\Xi_\alpha := \{\xi_{1,\alpha}, \xi_{2,\alpha}, \dots, \xi_{n_\alpha+p_\alpha+1,\alpha}\}$ consisting of nondecreasing *knots*, i.e., $\xi_{1,\alpha} \leq \xi_{2,\alpha} \leq \dots \leq \xi_{n_\alpha+p_\alpha+1,\alpha}$. Knots may be repeated with the number of repetitions called *multiplicity*. A knot vector is assumed to be *open*, i.e., both of the first and the last $p_\alpha + 1$ knots are repeated, where p_α is the polynomial degree. Let $B_{i,\alpha}$ ($i = 1, 2, \dots, n_\alpha$) denote B-spline basis functions, which are defined recursively as [14]

$$B_{i,0}(\xi) = \begin{cases} 1 & \text{if } \xi_i \leq \xi \leq \xi_{i+1}, \\ 0 & \text{otherwise,} \end{cases}$$

$$B_{i,\alpha}(\xi) = \frac{\xi - \xi_i}{\xi_{i+\alpha} - \xi_i} B_{i,\alpha-1}(\xi) + \frac{\xi_{i+\alpha+1} - \xi}{\xi_{i+\alpha+1} - \xi_{i+1}} B_{i+1,\alpha-1}(\xi).$$

Each B-spline basis function is everywhere pointwise C^∞ -continuous except at knots $\xi_{i,\alpha}$, where it is $C^{p_\alpha - \kappa_{i,\alpha}}$ -continuous if the multiplicity of the knot is $\kappa_{i,\alpha}$ with $1 \leq \kappa_{i,\alpha} < p_\alpha + 1$. The B-spline basis functions are non-negative, locally supported in $(\xi_{i,\alpha}, \xi_{i+p_\alpha+1,\alpha})$ (the *knot span*), and constitute a partition of unity [13], i.e., $\sum_{i=1}^{n_\alpha} B_{i,\alpha} = 1$. We define the space of univariate B-splines $\mathcal{B}_\alpha \equiv \mathcal{B}(\Xi_\alpha; p_\alpha) := \text{span}\{B_{i,\alpha}\}_{i=1, \dots, n_\alpha}$. An example of quadratic non-uniform B-spline is presented in Fig. 1. Note that basis functions are interpolatory at

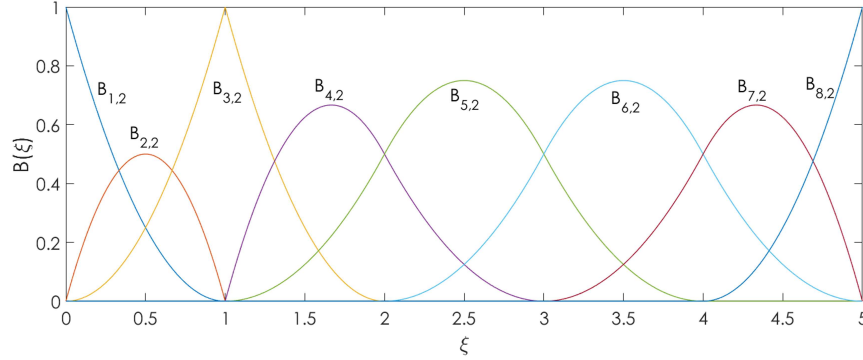


Figure 1: B-spline basis functions with knot vector. $\Xi_2 = \{0,0,0,1,1,2,3,4,5,5,5\}$.

$\xi = 0, \xi = 5$, and also at $\xi = 1$, the location of a repeated knot, where only C^0 -continuity is attained. Elsewhere the functions are C^1 -continuous.

Multivariate tensor product B-splines are defined based on d knot vectors Ξ_α , $\alpha = 1, \dots, d$. Let $\hat{\Omega} := (0,1)^d \subset \mathbb{R}^d$ be an open *parametric domain*. The knot vectors partition $\hat{\Omega}$ into “mesh” elements, which constitute a mesh $\mathcal{Q}_h \equiv \mathcal{Q}_h(\Xi_1, \dots, \Xi_d) := \{Q = \otimes_{\alpha=1}^d (\xi_{i_\alpha, \alpha}, \xi_{i_\alpha+1, \alpha}) \mid p_\alpha + 1 \leq i_\alpha \leq n_\alpha - 1\}$. Let us denote $\hat{h}_Q := \text{diam}(Q)$ for all $Q \in \mathcal{Q}_h$ and the global mesh size $\hat{h} := \max_{Q \in \mathcal{Q}_h} \{\hat{h}_Q\}$. For notational convenience, we denote a multi-index $\mathbf{i} := (i_1, \dots, i_d)$ and a corresponding multi-index set $I := \{\mathbf{i} = (i_1, \dots, i_d) \mid 1 \leq i_\alpha \leq n_\alpha \text{ for } 1 \leq \alpha \leq d\}$. Then, for each multi-index $\mathbf{i} \in I$, we define the tensor product B-spline basis functions $B_{\mathbf{i}}: \hat{\Omega} \rightarrow \mathbb{R}$, $B_{\mathbf{i}} := B_{i_1,1} \otimes \dots \otimes B_{i_d,d}$ and corresponding tensor product B-spline space:

$$\mathcal{B}_h \equiv \mathcal{B}_h(\Xi_1, \dots, \Xi_d; p_1, \dots, p_d) := \text{span}\{B_{\mathbf{i}}\}_{\mathbf{i} \in I}. \quad (2.3)$$

Notice that the functions in \mathcal{B}_h are piecewise polynomials of degree p_α along each coordinate α .

We associate the basis functions $B_{\mathbf{i}}$ with positive weights $\omega_{\mathbf{i}}$ and define a *weighting function* $\omega: \hat{\Omega} \rightarrow \mathbb{R}$, with $\omega := \sum_{\mathbf{i} \in I} \omega_{\mathbf{i}} B_{\mathbf{i}}$. The NURBS basis functions on the parameter patch are defined by projection:

$$R_{\mathbf{i}}: \hat{\Omega} \rightarrow \mathbb{R} \quad \text{with} \quad R_{\mathbf{i}} = \frac{\omega_{\mathbf{i}} B_{\mathbf{i}}}{\omega} \quad (2.4)$$

and the corresponding NURBS space reads: $\mathcal{S}_h \equiv \mathcal{S}_h(\Xi_1, \dots, \Xi_d; p_1, \dots, p_d; \omega) := \text{span}\{R_{\mathbf{i}}\}_{\mathbf{i} \in I}$.

In order to perform a parameterization of the physical domain, we introduce the control points $\mathbf{C}_{\mathbf{i}} \in \mathbb{R}^d$ and define the *geometric mapping* $\mathbf{F}: \hat{\Omega} \rightarrow \Omega$ with $\mathbf{F} := \sum_{\mathbf{i} \in I} \mathbf{C}_{\mathbf{i}} R_{\mathbf{i}}$. Let us assume that \mathbf{F} is invertible and possesses smooth inverse a.e. in each element $Q \in \mathcal{Q}_h$. We define $\nabla \mathbf{F}: \hat{\Omega} \rightarrow \mathbb{R}^d$ and $J_{\mathbf{F}}: \hat{\Omega} \rightarrow \mathbb{R}$ to be the Jacobian matrix and determinant of map \mathbf{F} , respectively. By using \mathbf{F} , we define a *physical mesh* in the physical domain Ω , whose elements are obtained as the image of the elements in the parametric domain, i.e.,

$\mathcal{K}_h := \{K = \mathbf{F}(Q) \mid Q \in \mathcal{Q}_h\}$. The corresponding mesh size in the physical domain is defined as $h := \max_{K \in \mathcal{K}_h} h_K$, where $h_K = \|\nabla \mathbf{F}\|_{L^\infty(Q)} h_Q$. Associated with a family of meshes $\{\mathcal{Q}_h\}_{h>0}$ in parametric domain $\widehat{\Omega}$, we introduce a family of meshes $\{\mathcal{K}_h\}_h$ in physical domain Ω .

Furthermore, we define the space spanned by NURBS basis functions in Ω as the push-forward of the space \mathcal{S}_h , which reads:

$$\mathcal{V}_h \equiv \mathcal{V}_h(p_1, \dots, p_\alpha) := \text{span}\{R_i \circ \mathbf{F}^{-1}\}_{i \in I} = \text{span}\{\mathcal{R}_i\}_{i \in I}, \quad (2.5)$$

where $\{\mathcal{R}_i\}_{i \in I}$ is the NURBS basis in the physical domain with $\mathcal{R}_i := R_i \circ \mathbf{F}^{-1}$ for all $i \in I$.

2.1.2 IGA semi-discretization

In a d -dimensional problem, define trial space $\mathcal{S} := \{\mathbf{v} \in H^1(\Omega)^d \mid \mathbf{v}|_{\Gamma_D} = \mathbf{g}\}$, and test spaces $\mathcal{V} := \{\mathbf{v} \in H^1(\Omega)^d \mid \mathbf{v}|_{\Gamma_D} = \mathbf{0}\}$. The variational form of (2.1) reads: find $\mathbf{u}(t) \in \mathcal{S}$, for $\forall \mathbf{v} \in \mathcal{V}$, such that

$$m(\mathbf{v}, \mathbf{u}(t)) + c(\mathbf{v}, \mathbf{u}(t)) + k(\mathbf{v}, \mathbf{u}(t)) = l(\mathbf{v}; t), \quad (2.6)$$

bilinear forms $m(\cdot, \cdot)$, $c(\cdot, \cdot)$, $k(\cdot, \cdot)$ and $l(\cdot; \cdot)$ are defined as follows:

$$\begin{cases} m(\mathbf{v}, \mathbf{u}) = \int_{\Omega} \rho \mathbf{v} \cdot \frac{\partial^2 \mathbf{u}}{\partial t^2} d\Omega, \\ c(\mathbf{v}, \mathbf{u}) = \int_{\Omega} 2\rho \zeta \mathbf{v} \cdot \frac{\partial \mathbf{u}}{\partial t} d\Omega, \\ k(\mathbf{v}, \mathbf{u}) = \int_{\Omega} \boldsymbol{\epsilon}(\mathbf{v}) : \boldsymbol{\sigma}(\mathbf{u}) d\Omega + \int_{\Omega} \rho \zeta^2 \mathbf{v} \cdot \mathbf{u} d\Omega, \\ l(\mathbf{v}; t) = \int_{\Omega} \mathbf{v} \cdot \mathbf{f}(t) d\Omega + \int_{\Gamma_N} \mathbf{v} \cdot \mathbf{h}(t) d\Omega. \end{cases} \quad (2.7)$$

We define finite-dimensional NURBS space $\mathcal{L}^h = \text{span}\{\mathcal{R}_i\}_{i \in I}^d$. Let us consider a finite-dimensional trial spaces $\mathcal{S}^h = \mathcal{L}^h \cap \mathcal{S} \subset \mathcal{S}$, and a finite-dimensional test space $\mathcal{V}^h = \mathcal{L}^h \cap \mathcal{V} \subset \mathcal{V}$. Then the finite-dimensional approximation of (2.6) reads: find $\mathbf{u}^h(t) \in \mathcal{S}^h$, for $\forall \mathbf{v}^h \in \mathcal{V}^h$, such that

$$m(\mathbf{v}^h, \mathbf{u}^h(t)) + c(\mathbf{v}^h, \mathbf{u}^h(t)) + k(\mathbf{v}^h, \mathbf{u}^h(t)) = l(\mathbf{v}^h; t). \quad (2.8)$$

For the sake of simplicity, we consider $d = 2$. Then, $\mathbf{f}(t) = (f_1(t), f_2(t))^T$, $\mathbf{g}(t) = (g_1(t), g_2(t))^T$, $\mathbf{h}(t) = (h_1(t), h_2(t))^T$, $\mathbf{u}^h(t) = (u_1^h(t), u_2^h(t))^T$ and $\mathbf{v}^h = (v_1^h, v_2^h)^T$. In the finite dimensional space, $u_1^h(t)$ and $u_2^h(t)$ can be represented by: $u_1^h(t) = \sum_{i=1}^{N_d} c_{u,1,i}(t) \mathcal{R}_i$ and $u_2^h(t) = \sum_{i=1}^{N_d} c_{u,2,i}(t) \mathcal{R}_i$, where $\mathbf{c}_{u,1}(t) = \{c_{u,1,i}(t)\}_{i=1 \dots N_d} \in \mathbb{R}^{N_d}$ and $\mathbf{c}_{u,2}(t) = \{c_{u,2,i}(t)\}_{i=1 \dots N_d} \in \mathbb{R}^{N_d}$ are the NURBS control variables of $u_1^h(t)$ and $u_2^h(t)$. Define the vectorial control variable of \mathbf{u}^h : $\mathbf{U}(t) = (c_{u,1}(t), c_{u,2}(t))^T$, the control variables of $\frac{\partial^2 \mathbf{u}^h}{\partial t^2}(t)$ and $\frac{\partial \mathbf{u}^h}{\partial t}(t)$, $\mathbf{U}''(t)$ and $\mathbf{U}'(t)$ are defined in the same manner. Substitute them into (2.8),

and let v_1^h and v_2^h take over all basis functions of \mathcal{V}_1^h and \mathcal{V}_2^h . We have the following linear system:

$$\mathbf{M}\mathbf{U}''(t) + \mathbf{C}\mathbf{U}'(t) + \mathbf{K}\mathbf{U}(t) = \mathbf{F}(t), \quad (2.9)$$

where matrices $\mathbf{M}, \mathbf{C}, \mathbf{K} \in \mathbb{R}^{2N_d \times 2N_d}$ and $\mathbf{F}(t) \in \mathbb{R}^{2N_d}$ are defined

$$\mathbf{M} = \begin{pmatrix} \mathbf{M}_{11} & \mathbf{0} \\ \mathbf{0} & \mathbf{M}_{22} \end{pmatrix}, \quad \mathbf{C} = \begin{pmatrix} \mathbf{C}_{11} & \mathbf{0} \\ \mathbf{0} & \mathbf{C}_{22} \end{pmatrix}, \quad \mathbf{K} = \begin{pmatrix} \mathbf{K}_{11} & \mathbf{K}_{12} \\ \mathbf{K}_{21} & \mathbf{K}_{22} \end{pmatrix}, \quad \mathbf{F}(t) = \begin{pmatrix} \mathbf{F}_1(t) \\ \mathbf{F}_2(t) \end{pmatrix}, \quad (2.10)$$

in which matrices $\mathbf{M}_{11}, \mathbf{M}_{22}, \mathbf{C}_{11}, \mathbf{C}_{22}, \mathbf{K}_{11}, \mathbf{K}_{12}, \mathbf{K}_{21}, \mathbf{K}_{22} \in \mathbb{R}^{N_d \times N_d}$ and vectors $\mathbf{F}_1(t), \mathbf{F}_2(t) \in \mathbb{R}^{N_d}$ are obtained with entries from following integrals by means of suitable quadrature rules:

$$\left\{ \begin{array}{l} \{\mathbf{M}_{11}\}_{i,j} = \{\mathbf{M}_{22}\}_{i,j} = \int_{\Omega} \rho \mathcal{R}_i \mathcal{R}_j d\Omega, \\ \{\mathbf{C}_{11}\}_{i,j} = \{\mathbf{C}_{22}\}_{i,j} = \int_{\Omega} 2\rho\zeta \mathcal{R}_i \mathcal{R}_j d\Omega, \\ \{\mathbf{K}_{11}\}_{i,j} = \int_{\Omega} (\lambda + 2\mu) \frac{\partial \mathcal{R}_i}{\partial x} \frac{\partial \mathcal{R}_j}{\partial x} + \frac{1}{2}\mu \left(\frac{\partial \mathcal{R}_i}{\partial y} \frac{\partial \mathcal{R}_j}{\partial y} + \frac{\partial \mathcal{R}_i}{\partial x} \frac{\partial \mathcal{R}_j}{\partial y} \right) + \rho\zeta^2 \mathcal{R}_i \mathcal{R}_j d\Omega, \\ \{\mathbf{K}_{12}\}_{i,j} = \int_{\Omega} \lambda \frac{\partial \mathcal{R}_i}{\partial x} \frac{\partial \mathcal{R}_j}{\partial y} + \frac{1}{2}\mu \left(\frac{\partial \mathcal{R}_i}{\partial y} \frac{\partial \mathcal{R}_j}{\partial x} + \frac{\partial \mathcal{R}_i}{\partial x} \frac{\partial \mathcal{R}_j}{\partial x} \right) d\Omega, \\ \{\mathbf{K}_{21}\}_{i,j} = \int_{\Omega} \lambda \frac{\partial \mathcal{R}_i}{\partial y} \frac{\partial \mathcal{R}_j}{\partial x} + \frac{1}{2}\mu \left(\frac{\partial \mathcal{R}_i}{\partial x} \frac{\partial \mathcal{R}_j}{\partial y} + \frac{\partial \mathcal{R}_i}{\partial y} \frac{\partial \mathcal{R}_j}{\partial y} \right) d\Omega, \\ \{\mathbf{K}_{22}\}_{i,j} = \int_{\Omega} (\lambda + 2\mu) \frac{\partial \mathcal{R}_i}{\partial y} \frac{\partial \mathcal{R}_j}{\partial y} + \frac{1}{2}\mu \left(\frac{\partial \mathcal{R}_i}{\partial x} \frac{\partial \mathcal{R}_j}{\partial x} + \frac{\partial \mathcal{R}_i}{\partial y} \frac{\partial \mathcal{R}_j}{\partial x} \right) + \rho\zeta^2 \mathcal{R}_i \mathcal{R}_j d\Omega, \\ \{\mathbf{F}_1(t)\}_{i,j} = \int_{\Omega} \mathcal{R}_i f_1(t) d\Omega + \int_{\Gamma_N} \mathcal{R}_i h_1 d\Omega, \\ \{\mathbf{F}_2(t)\}_{i,j} = \int_{\Omega} \mathcal{R}_i f_2(t) d\Omega + \int_{\Gamma_N} \mathcal{R}_i h_2 d\Omega, \end{array} \right. \quad (2.11)$$

notice that integrals in (2.11) need to be computed on the parametric domain.

2.2 Temporal discretization

2.2.1 Generalized- α method

Now we discretize (2.9) in time by means of the generalized- α method [16, 19]. Let us denote acceleration \mathbf{U}'' as \mathbf{a} , velocity \mathbf{U}' as \mathbf{v} and displacement \mathbf{U} as \mathbf{d} . Relations between \mathbf{a} , \mathbf{v} and \mathbf{d} , fully discretized function, time discretization scheme and initial condition are:

$$\left\{ \begin{array}{l} \mathbf{d}_{n+1} = \mathbf{d}_n + \Delta t \mathbf{v}_n + \Delta t^2 \left[\left(\frac{1}{2} - \beta \right) \mathbf{a}_n + \beta \mathbf{a}_{n+1} \right], \\ \mathbf{v}_{n+1} = \mathbf{v}_n + \Delta t \left[(1 - \gamma) \mathbf{a}_n + \gamma \mathbf{a}_{n+1} \right], \\ \mathbf{M} \mathbf{a}_{n+1 - \alpha_m} + \mathbf{C} \mathbf{v}_{n+1 - \alpha_f} + \mathbf{K} \mathbf{d}_{n+1 - \alpha_f} = \mathbf{F}(t_{n+1 - \alpha_f}), \end{array} \right. \quad (2.12)$$

$$\begin{cases} \mathbf{d}_{n+1-\alpha_f} = (1-\alpha_f)\mathbf{d}_{n+1} + \alpha_f\mathbf{d}_n, \\ \mathbf{v}_{n+1-\alpha_f} = (1-\alpha_f)\mathbf{v}_{n+1} + \alpha_f\mathbf{v}_n, \\ \mathbf{a}_{n+1-\alpha_m} = (1-\alpha_m)\mathbf{a}_{n+1} + \alpha_m\mathbf{a}_n, \\ t_{n+1-\alpha_f} = (1-\alpha_f)t_{n+1} + \alpha_ft_n, \end{cases} \quad (2.13)$$

and

$$\begin{cases} \mathbf{d}_0 = \mathbf{U}_0, \\ \mathbf{v}_0 = \mathbf{U}'_0, \\ \mathbf{a}_0 = \mathbf{M}^{-1}(\mathbf{F}(0) - \mathbf{C}\mathbf{U}'_0 - \mathbf{K}\mathbf{U}_0), \end{cases} \quad (2.14)$$

where α_m , α_f , β and γ are given parameters. It is second-order accurate when $\gamma = \frac{1}{2} - \alpha_m + \alpha_f$ and unconditionally stable when $\alpha_m \leq \alpha_f \leq \frac{1}{2}$ and $\beta \geq \frac{1}{4} + \frac{1}{2}(\alpha_f - \alpha_m)$. High-frequency dissipation is maximized when $\beta = \frac{1}{4}(1 - \alpha_m + \alpha_f)$, and low-frequency dissipation is minimized when $\alpha_f = \frac{1+\alpha_m}{3}$. Then, we introduce a parameter $\rho_\infty \in [0,1]$ [16] to control the high frequency damping. For a linear problem, the greater the ρ_∞ , the less high-frequency damping. To avoid unexpected instabilities while retaining a certain amount of high-frequency information, we select $\rho_\infty = 0.5$ and set

$$\alpha_m = \frac{2\rho_\infty - 1}{\rho_\infty + 1}, \quad \alpha_f = \frac{\rho_\infty}{\rho_\infty + 1}, \quad \beta = \frac{1}{(\rho_\infty + 1)^2}, \quad \gamma = \frac{3 - \rho_\infty}{2(\rho_\infty + 1)}. \quad (2.15)$$

2.2.2 Full discretization for snapshots

Substitute (2.13) into the last equation of (2.12) and we have

$$\begin{aligned} & (1-\alpha_m)\mathbf{M}\mathbf{a}_{n+1} + (1-\alpha_f)\mathbf{C}\mathbf{v}_{n+1} + (1-\alpha_f)\mathbf{K}\mathbf{d}_{n+1} \\ & = \mathbf{F}((1-\alpha_f)t_{n+1} + \alpha_ft_n) - \alpha_m\mathbf{M}\mathbf{a}_n - \alpha_f\mathbf{C}\mathbf{v}_n - \alpha_f\mathbf{K}\mathbf{d}_n. \end{aligned} \quad (2.16)$$

Considering the Dirichlet boundary condition, we replace the first two equations of (2.12) with

$$\begin{cases} \mathbf{v}_{n+1} = a_1\mathbf{d}_{n+1} + a_2\mathbf{d}_n + a_3\mathbf{v}_n + a_4\mathbf{a}_n, \\ \mathbf{a}_{n+1} = b_1\mathbf{d}_{n+1} + b_2\mathbf{d}_n + b_3\mathbf{v}_n + b_4\mathbf{a}_n, \end{cases} \quad (2.17)$$

where

$$\begin{cases} a_1 = \frac{\gamma}{\beta\Delta t}, \\ a_2 = -\frac{\gamma}{\beta\Delta t}, \\ a_3 = 1 - \frac{\gamma}{\beta}, \\ a_4 = \Delta t(1-\gamma) - \Delta t\gamma\frac{1-2\beta}{2\beta} \end{cases} \quad \text{and} \quad \begin{cases} b_1 = \frac{1}{\beta\Delta t^2}, \\ b_2 = -\frac{1}{\beta\Delta t^2}, \\ b_3 = \frac{1}{\beta\Delta t}, \\ b_4 = -\frac{1-2\beta}{2\beta}. \end{cases} \quad (2.18)$$

Then substitute (2.17) into (2.16), we have the following linear system for snapshots of elastic wave problem:

$$\mathbf{M}_L \mathbf{d}_{n+1} = \mathbf{F}_R, \quad (2.19)$$

where

$$\begin{cases} \mathbf{M}_L = (1 - \alpha_m) b_1 \mathbf{M} + (1 - \alpha_f) a_1 \mathbf{C} + (1 - \alpha_f) \mathbf{K}, \\ \mathbf{F}_R = \mathbf{F}((1 - \alpha_f) t_{n+1} + \alpha_f t_n) - \mathbf{M}_{R_3} \mathbf{a}_n - \mathbf{M}_{R_2} \mathbf{v}_n - \mathbf{M}_{R_1} \mathbf{d}_n, \end{cases} \quad (2.20)$$

with

$$\begin{cases} \mathbf{M}_{R_1} = \left((1 - \alpha_m) b_2 \mathbf{M} + (1 - \alpha_f) a_2 \mathbf{C} + \alpha_f \mathbf{K} \right) \mathbf{d}_n, \\ \mathbf{M}_{R_2} = \left((1 - \alpha_m) b_3 \mathbf{M} + (1 - \alpha_f) a_3 \mathbf{C} + \alpha_f \mathbf{C} \right) \mathbf{d}_n, \\ \mathbf{M}_{R_3} = \left((1 - \alpha_m) b_4 \mathbf{M} + (1 - \alpha_f) a_4 \mathbf{C} + \alpha_m \mathbf{M} \right) \mathbf{d}_n. \end{cases} \quad (2.21)$$

Solving (2.19) with \mathbf{d}^n , \mathbf{v}^n and \mathbf{a}^n , we have displacement \mathbf{d}^{n+1} at next time step. Then \mathbf{v}^{n+1} and \mathbf{a}^{n+1} can be obtained.

2.3 Fully discretization for POD

2.3.1 Proper orthogonal decomposition

A numerical snapshot of (2.1) can be computed from (2.19). Generally, snapshots contain less time slices (greater time step) or smaller time span than the final numerical solution. Then we extract key information from the snapshots we got and build reduced basis model from it. Supposing we have snapshots

$$\{\mathbf{y}_j \mid \mathbf{y}_j = \mathbf{u}_j^h, j = 1, \dots, N\}. \quad (2.22)$$

Denote $\mathcal{V}_R := \text{span}\{\mathbf{y}_j \mid \mathbf{y}_j = \mathbf{u}_j^h, j = 1, \dots, N\}$ and $R := \dim \mathcal{V}_R \leq N < \infty$ (in some instances $R < N$ since in principle snapshots may be linearly dependent). For $N_r \in \{1, \dots, R\}$, POD requires to solve a finite-dimensional optimization problem

$$\begin{aligned} & \min_{\{\boldsymbol{\psi}_k\}_{k=1}^{N_r}} \frac{1}{N} \sum_{j=1}^N \left\| \mathbf{y}_j - \sum_{k=1}^{N_r} (\mathbf{y}_j, \boldsymbol{\psi}_k) \boldsymbol{\psi}_k \right\|^2 \\ & \text{subject to } (\boldsymbol{\psi}_i, \boldsymbol{\psi}_j) = \delta_{ij} \text{ for } 1 \leq i, j \leq N_r \end{aligned} \quad (2.23)$$

to obtain an optimal orthonormal basis $\{\boldsymbol{\psi}_i\}_{i=1}^{N_r}$ of V_r with $V_r \subset \mathcal{V}_R$. Then we introduce the *correlation matrix*

$$\mathcal{D} = [\mathcal{D}_{ij}] \in \mathbb{R}^{N \times N} \quad \text{with} \quad \mathcal{D}_{ij} = \frac{1}{N} (\mathbf{y}_j, \mathbf{y}_i), \quad (2.24)$$

which is symmetric positive semi-definite and has rank R since $\dim \mathcal{V}_R = R$. POD then requires to solve the following eigenvalue problem

$$\mathcal{D} \boldsymbol{\zeta} = \lambda \boldsymbol{\zeta}, \quad (2.25)$$

where $\mathcal{D} = DD^T W$ with D denoting the snapshot matrix whose columns corresponding to coefficients of the snapshots obtained by isogeometric analysis, and W denoting the mass matrix of isogeometric analysis associated with the $L^2(\Omega)$ inner product. Let $\lambda_1 \geq \dots \geq \lambda_R > 0$ denote the nonzero eigenvalues of \mathcal{D} , $\lambda_{R+1} = \dots = \lambda_N = 0$ the null ones, and $\mathbf{v}_1, \dots, \mathbf{v}_N \in \mathbb{R}^N$ be the associated eigenvectors. Then we have POD basis of rank N_r , $1 \leq N_r \leq R$:

$$\boldsymbol{\psi}_k = \frac{1}{\sqrt{N\lambda_k}} \sum_{n=1}^N \mathbf{v}_k \mathbf{u}_n^h, \quad k=1, \dots, N_r.$$

We have the following error formula from [9]:

$$\frac{1}{N} \sum_{n=1}^N \|\mathbf{u}_n^h - \mathbf{P}_r \mathbf{u}_n^h\|^2 = \sum_{k=N_r+1}^R \lambda_k \|\boldsymbol{\psi}_k\|^2.$$

Let $V_r = \text{span}\{\boldsymbol{\psi}_i\}_{i=1}^{N_r}$. The L^2 projection $\mathbf{P}_r: \mathcal{S}^h \rightarrow V_r$ is defined as

$$\mathbf{P}_r \mathbf{u}_n^h := \sum_{k=1}^{N_r} (\mathbf{u}_n^h, \boldsymbol{\psi}_k) \boldsymbol{\psi}_k, \quad \forall \mathbf{u}_n^h \in \mathcal{S}^h.$$

2.3.2 IGA-POD fully-discretization

Suppose we already have snapshots $\{\mathbf{d}_1, \mathbf{d}_2, \dots, \mathbf{d}_N\}$ using IGA. For easy treatment of boundary condition, we replace every \mathbf{d}_i with $\bar{\mathbf{d}}_i = \mathbf{d}_i - \bar{\mathbf{d}}$, $i = 1, 2, \dots, N$, where $\bar{\mathbf{d}} = (\sum_{i=1}^N \mathbf{d}_i) / N$ is the average of snapshots. We set weight matrix:

$$W = \begin{pmatrix} W_m & 0 \\ 0 & W_m \end{pmatrix}, \quad (2.26)$$

where $\{W_m\}_{i,j} = \int_{\Omega} \mathcal{R}_i \mathcal{R}_j d\Omega \in \mathbb{R}^{N_d \times N_d}$, and $\Theta = \Delta t \times \text{diag}(0.5, 1, 1, \dots, 1, 0.5) \in \mathbb{R}^{N \times N}$. For a m -dimensional problem, $N_{\text{dof}} = mN_d$. Now we have averaged snapshots $D = \{\bar{\mathbf{d}}_1, \bar{\mathbf{d}}_2, \dots, \bar{\mathbf{d}}_N\} \in \mathbb{R}^{N_{\text{dof}} \times N}$, diagonal matrix $\Theta \in \mathbb{R}^{N \times N}$ and weight matrix $W \in \mathbb{R}^{N_{\text{dof}} \times N_{\text{dof}}}$, following the procedure in Algorithm 1, we have POD modes $\{\boldsymbol{\psi}_i\} \in \mathbb{R}^{N_{\text{dof}} \times N}$.

Given an error tolerance $\epsilon_{\text{tol}} > 0$, the number of reduced basis N_r is determined by choosing minimal N_r such that

$$\frac{\sum_{i=1}^{N_r} \lambda_i}{\sum_{i=1}^N \lambda_i} > 1 - \epsilon_{\text{tol}}. \quad (2.27)$$

Then we have the order reduced basis: $\mathbf{P}_r = (\boldsymbol{\psi}_1, \boldsymbol{\psi}_2, \dots, \boldsymbol{\psi}_{N_r}) \in \mathbb{R}^{N_{\text{dof}} \times N_r}$ with $N_r \ll N$. We reduce the order of (2.19) using \mathbf{P}_r and have the following linear system:

$$\tilde{\mathbf{M}}_L \tilde{\mathbf{d}}_{n+1} = \tilde{\mathbf{F}}_R, \quad (2.28)$$

where the reduced order matrix $\tilde{\mathbf{M}}_L \in \mathbb{R}^{N_r \times N_r}$ and the reduced order vector $\tilde{\mathbf{F}}_R \in \mathbb{R}^{N_r}$ are

$$\begin{cases} \tilde{\mathbf{M}}_L = \mathbf{P}_r^T \mathbf{M}_L \mathbf{P}_r \\ \tilde{\mathbf{F}}_R = \mathbf{P}_r^T \mathbf{F}((1 - \alpha_f)t_{n+1} + \alpha_f t_n) - \mathbf{P}_r^T \mathbf{M}_{R_3} \mathbf{P}_r \tilde{\mathbf{a}}_n - \mathbf{P}_r^T \mathbf{M}_{R_2} \mathbf{P}_r \tilde{\mathbf{v}}_n \\ \quad - \mathbf{P}_r^T \mathbf{M}_{R_1} \mathbf{P}_r (\bar{\mathbf{d}}_n + \bar{\mathbf{d}}) - \mathbf{P}_r^T \mathbf{M}_L \bar{\mathbf{d}}. \end{cases} \quad (2.29)$$

Algorithm 1 Compute PGD modes from snapshots**Require:** D, W, Θ

- 1: **case** $N_{dof} < N$:
- 2: $\bar{D} = W^{1/2} D \Theta^{1/2}$
- 3: $R = \bar{D} \bar{D}^T \in \mathbb{R}^{N_{dof} \times N_{dof}}$
- 4: $R = \bar{\Psi} \Lambda \bar{\Psi}^T$
- 5: $\psi_i = W^{-1/2} \bar{\Psi}(:, i) \in \mathbb{R}^{N_{dof}}$
- 6: $\lambda_i = \Lambda_{ii}$ for $i = 1, \dots, N$
- 7: **case** $N_{dof} = N$:
- 8: $\bar{D} = W^{1/2} D \Theta^{1/2}$
- 9: $\bar{D} = \bar{\Psi} \Sigma \bar{\Phi}^T$
- 10: $\psi_i = W^{-1/2} \bar{\Psi}(:, i) \in \mathbb{R}^{N_{dof}}$
- 11: $\lambda_i = \Sigma_{ii}^2$ for $i = 1, \dots, N$
- 12: **case** $N_{dof} > N$:
- 13: $K = \Theta^{1/2} D^T W D \Theta^{1/2}$
- 14: $K = \bar{\Phi} \Lambda \bar{\Phi}^T$
- 15: $\psi_i = D \Theta^{1/2} \bar{\Phi}(:, i) / \sqrt{\lambda_i} \in \mathbb{R}^{N_{dof}}$
- 16: $\lambda_i = \Lambda_{ii}$ for $i = 1, \dots, N$
- 17: **return** POD modes $\{\psi_i\}$ and eigenvalues $\{\lambda_i\}$.

The recovering of \tilde{v} and \tilde{a} from \tilde{d} are defined as follows:

$$\begin{cases} \tilde{v}_{n+1} = a_1 \tilde{d}_{n+1} + a_2 \tilde{d}_n + a_3 \tilde{v}_n + a_4 \tilde{a}_n, \\ \tilde{a}_{n+1} = b_1 \tilde{d}_{n+1} + b_2 \tilde{d}_n + b_3 \tilde{v}_n + b_4 \tilde{a}_n. \end{cases} \quad (2.30)$$

For the initial condition, we perform a least-square projection from $\mathbb{R}^{N_{dof}}$ to \mathbb{R}^{N_r} :

$$\begin{cases} \tilde{d}_0 = (P_r^T P_r)^{-1} (P_r^T d_0), \\ \tilde{v}_0 = (P_r^T P_r)^{-1} (P_r^T v_0), \\ \tilde{a}_0 = (P_r^T P_r)^{-1} (P_r^T a_0). \end{cases} \quad (2.31)$$

Then by solving (2.28), we obtain reduced order solutions $\tilde{U}'' = \{\tilde{a}_i\}$, $\tilde{U}' = \{\tilde{v}_i\}$, $\tilde{U} = \{\tilde{d}_i\} \in \mathbb{R}^{N_r \times N_p}$. Finally POD solution can be recovered from reduced order solution: $U_r'' = P_r \tilde{U}''$, $U_r' = P_r \tilde{U}'$ and $U_r = P_r \tilde{U} + (\tilde{d}, \tilde{d}, \dots, \tilde{d})$. Notice that $N_p \neq N$, and POD time size is not necessarily the same as that for obtaining snapshot. When snapshots and POD have different time steps, coefficients a_1 to a_4 , b_1 to b_4 in (2.30) need to be re-computed.

3 Numerical errors

We have presented a detailed IGA-POD algorithm and work flow for the elastic wave problem. Now, we are going to examine the accuracy of our method. In the following

parts, numerical errors will be analyzed from two different aspects: numerical dispersion and numerical convergence.

3.1 Numerical dispersion

In dispersion analysis, we are interested in the error between numerical wave length and exact wave length. Numerical dispersion for elastodynamics with isogeometric Galerkin method are considered in [12,13]. Both isotropic and anisotropic dispersion for 2D elastic wave with IGA-Galerkin are shown in [20]. 2D and 3D isotropic numerical dispersion for elastic wave with spectral element method are studied in [21]. From these studies we find that IGA possesses better dispersion behavior than finite element method and spectral element method. For the sake of brevity, numerical dispersion for snapshots will not be included here, we refer [20,21] for details. General idea of dispersion analysis considers a specific solution of (2.1) in the form of harmonic waves function:

$$\mathbf{H} = \mathbf{\Psi} e^{i\mathbf{k}\cdot\mathbf{x} - i\omega t}, \quad (3.1)$$

where $\mathbf{\Psi}$ is the amplitude of the wave, $\mathbf{k} = 2\pi k_h (\cos(\theta), \sin(\theta))^T$ is the wave vector and ω is the angular velocity. Then a discrete wave solution is combined with the discrete elastic wave function into a discrete eigenvalue problem that yields compressional and shear wave velocity. However, this technique is not compatible with POD. POD extracts information from snapshots which are obtained from a time-dependent problem. Moreover, eigenvalue problem neglects the temporal structure. Instead of considering errors on velocity or wavelength, therefore we consider L^2 error between Snapshot, POD solution and exact solution with respect to different wave number and other parameters.

Consider the elastic wave function (2.1) in a square $\Omega = (0,1)^2$ with $\zeta = 0$, $T = 5 \times 10^{-2}$, $\Delta t = 10^{-3}$ and inhomogeneous Dirichlet boundary condition $\mathbf{u} = \mathbf{H}$, on Γ_D . Substituting (3.1) into (2.1) we have $f = \rho \frac{\partial^2 \mathbf{H}}{\partial t^2} - \nabla \cdot \boldsymbol{\sigma}(\mathbf{H})$. Then we set two different configurations for this problem: First we consider the function that describes compressional wave. Denote $\mathbf{e}_k = \frac{\mathbf{k}}{|\mathbf{k}|}$ the unit vector of \mathbf{k} and \mathbf{n}_k the unit normal vector of \mathbf{k} . We set $\mathbf{\Psi} = \mathbf{e}_k$ and $\omega = k_h c_p$. Then for the shear wave we set $\mathbf{\Psi} = \mathbf{n}_k$ and $\omega = k_h c_s$.

Next let us compare the effect of regularity on the error. We consider four cases of NURBS basis functions with the same polynomial degrees $p=4$ but different regularities: $k=0$, $k=1$, $k=2$ and $k=3$. In order to ensure that the number of degrees of freedom for different problems using each basis functions is consistent with each other, we introduce different mesh subdivisions for different problems: 13×13 meshes for $k=3$, 7×7 meshes for $k=2$, 5×5 mesh for $k=1$ and 4×4 mesh for $k=0$. Now number of degrees of freedom $N_{dof} = 2N_d = 578 = 2 \times 17^2$. Now use these basis functions in turn to solve the elastic wave problem above. Let the POD time step to be the same as that in obtaining snapshot, $\nu = 0.4$, $\theta = 0$ or $\theta = \frac{\pi}{4}$, $H = \frac{k_h}{17}$, $\epsilon_{tol} = 10^{-8}$, and consider the compressional wave case. We denote the L^2 error at time $t = 5 \times 10^{-2}$ between a POD solution and the exact solution by E_p , and the L^2 error at time $t = 5 \times 10^{-2}$ between a POD solution and a snapshot by $E_{p,r}$. E_p and $E_{p,r}$ with respect to H are shown in Figs. 2-3.

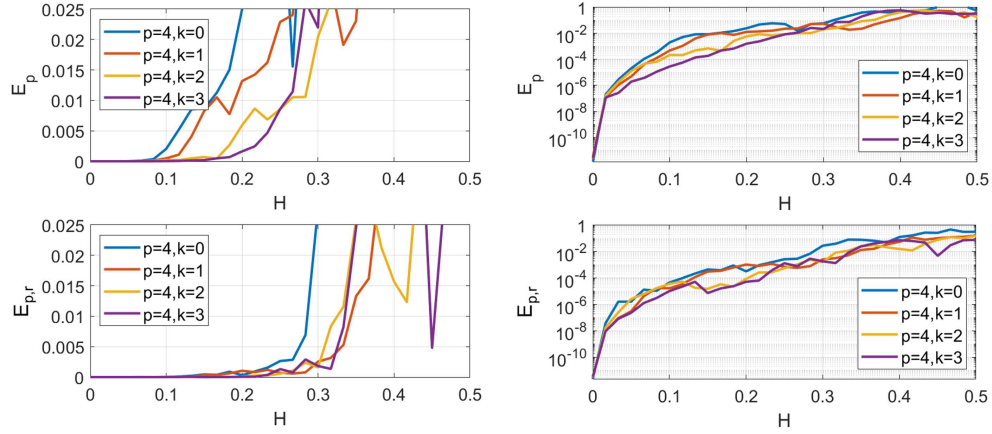


Figure 2: L^2 error between POD solution and exact solution (top left and top right), L^2 error between snapshot and POD solution (bottom left and bottom right), with respect to $k(p=4)$, for compressional wave at $\theta=0$ and $\nu=0.4$.

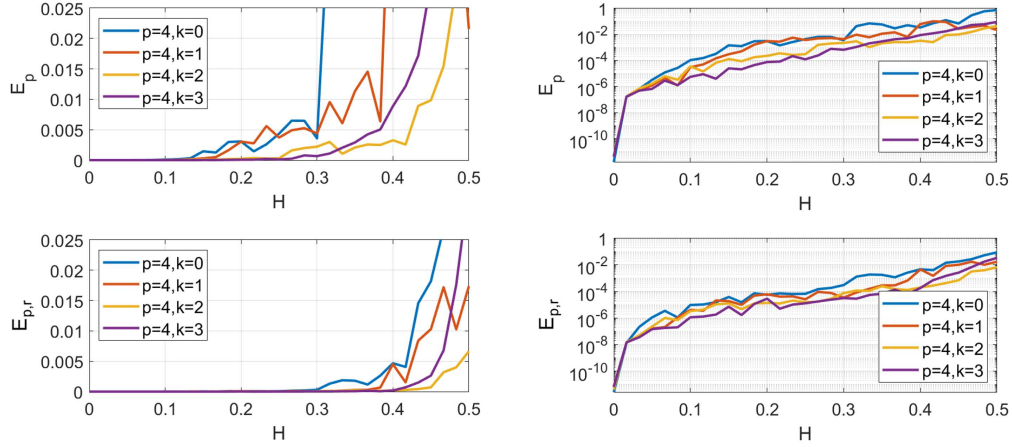


Figure 3: L^2 error between POD solution and exact solution (top left and top right), L^2 error between snapshot and POD solution (bottom left and bottom right), with respect to $k(p=4)$, for compressional wave at $\theta=\frac{\pi}{4}$ and $\nu=0.4$.

Then consider the shear wave case. Denote the L^2 error at time $t=5 \times 10^{-2}$ between a POD solution and the exact solution by E_s , and L^2 error at time $t=5 \times 10^{-2}$ between a POD solution and a snapshot by $E_{s,r}$, E_s and $E_{s,r}$ with respect to H are shown in Figs. 4-5.

Now let us compare the effect of polynomial degree on the error. Considering 4 new types of NURBS basis functions that all have maximum regularity but different polynomial degrees: $(p=1, k=0)$, $(p=2, k=1)$, $(p=3, k=2)$ and $(p=4, k=3)$. Set 13×13 meshes for $(p=4, k=3)$, 14×14 meshes for $(p=3, k=2)$, 15×15 mesh for $(p=2, k=1)$ and 16×16 mesh for $(p=1, k=0)$ so that $N_{dof} = 578$. $E_p, E_{p,r}, E_s$ and $E_{s,r}$ all have the same definition as that before. The results are shown in Figs. 6-9.

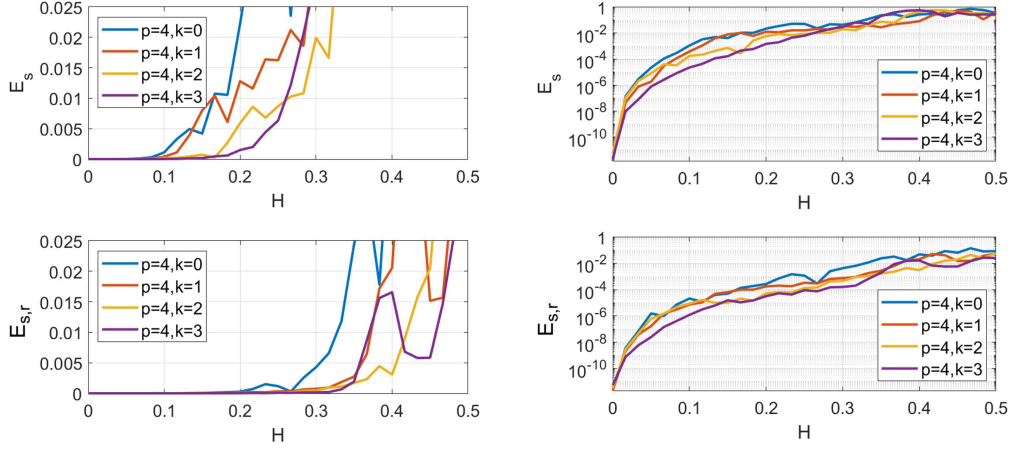


Figure 4: L^2 error between POD solution and exact solution (top left and top right), L^2 error between snapshot and POD solution (bottom left and bottom right), with respect to $k(p=4)$, for shear wave at $\theta=0$ and $\nu=0.4$.

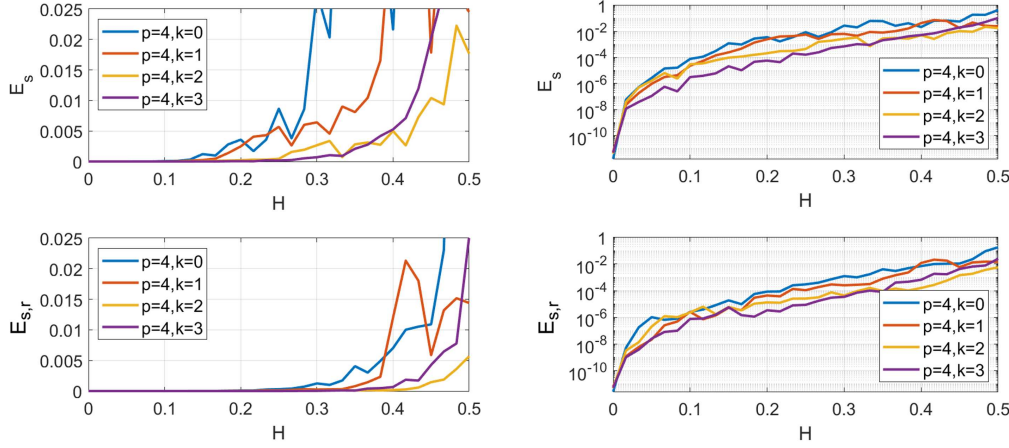


Figure 5: L^2 error between POD solution and exact solution (top left and top right), L^2 error between snapshot and POD solution (bottom left and bottom right), with respect to $k(p=4)$, for shear wave at $\theta=\frac{\pi}{4}$ and $\nu=0.4$.

Finally we consider the effect of the direction of wave vector on the error. We fix $H=0.25$, then let θ take over 0 to 2π . For each θ , we amplify current E_p and E_s to $1+25E_p$ and $1+25E_s$, then the error figure of the value in polar coordinates for both compressional wave and shear wave are given in Fig. 10.

By comparing figures of $\theta=0$ to figures of $\theta=\frac{\pi}{4}$, we find that for basis functions of any regularity and polynomial degree, the numerical error is greatly related to the angle of the wave vector. When $\theta=\frac{\pi}{4}$, both the accuracy of the numerical solution and the range of maintaining high precision are far better than the case where $\theta=0$. This phenomenon is particularly evident on basis functions with $k>0$. After all, when $k=0$, the basis functions no longer meet the requirements of the trial space and test space. The

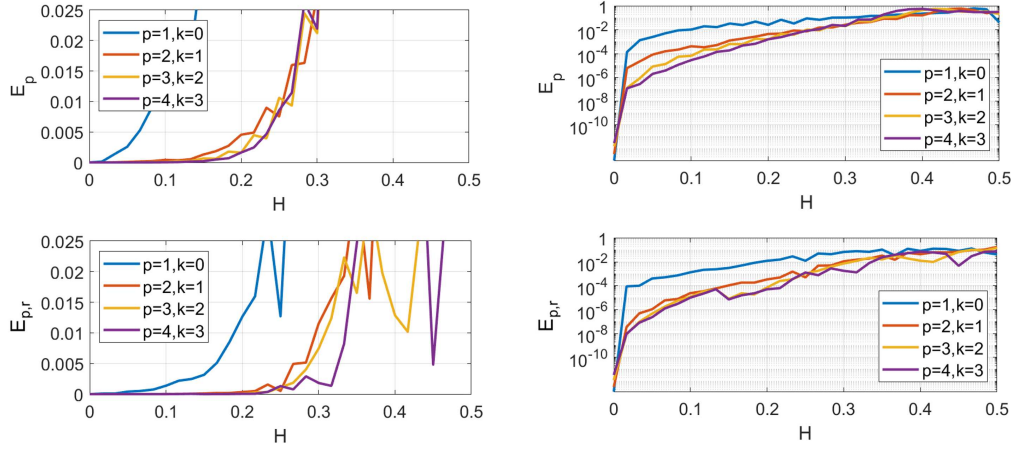


Figure 6: L^2 error between POD solution and exact solution (top left and top right), L^2 error between snapshot and POD solution (bottom left and bottom right), with respect to p and k , for compressional wave at $\theta=0$ and $\nu=0.4$.

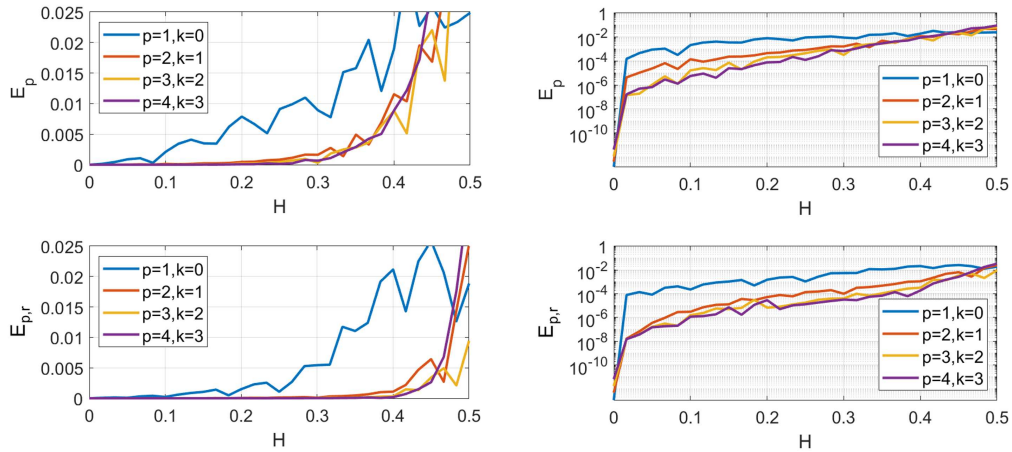


Figure 7: L^2 error between POD solution and exact solution (top left and top right), L^2 error between snapshot and POD solution (bottom left and bottom right), with respect to p and k , for compressional wave at $\theta=\frac{\pi}{4}$ and $\nu=0.4$.

relationship between error and θ can be better reflected in Fig. 10. From this figure we can find error at $\theta=0, \frac{\pi}{2}, \pi, \frac{3\pi}{2}$ are greater than that at $\theta=\frac{\pi}{4}, \frac{3\pi}{4}, \frac{5\pi}{4}, \frac{7\pi}{4}$. Therefore, in the actual situation, when selecting the mesh size according to the wave number, the horizontal or vertical wave is usually considered first. Next, we compare the effects of regularity and polynomial degree on the error. From the figure, we can find that under the same number of degree of freedom, basis functions with higher regularity and polynomial degree control the numerical error better. Although when H is large enough (usually $H > 0.3$), the error of the high-regularity basis function may even be greater than other

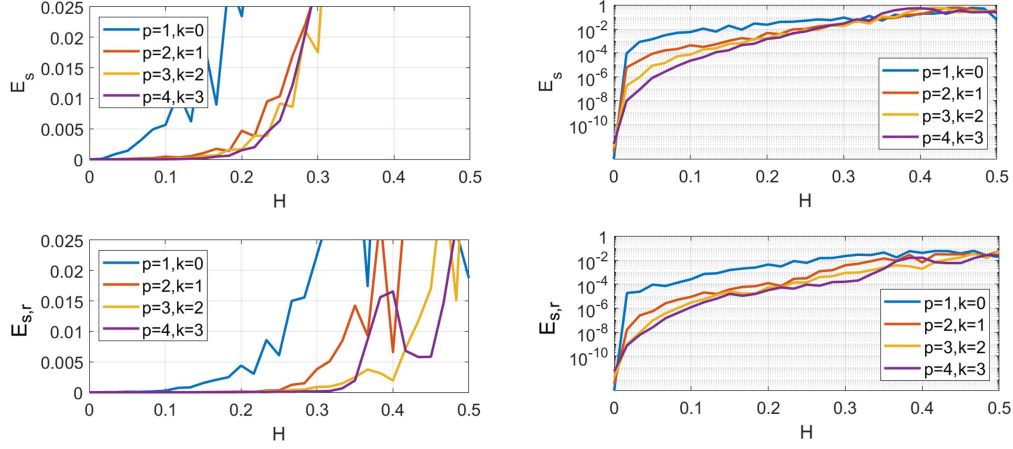


Figure 8: L^2 error between POD solution and exact solution (top left and top right), L^2 error between snapshot and POD solution (bottom left and bottom right), with respect to p and k , for shear wave at $\theta=0$ and $\nu=0.4$.

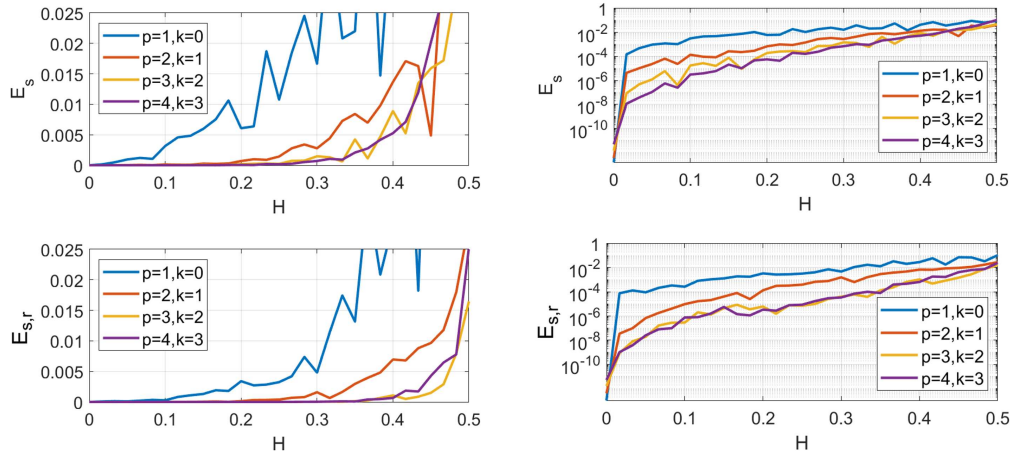


Figure 9: L^2 error between POD solution and exact solution (top left and top right), L^2 error between snapshot and POD solution (bottom left and bottom right), with respect to p and k , for shear wave at $\theta=\frac{\pi}{4}$ and $\nu=0.4$.

basis functions. But a grid that can make H so large is usually not used in practice so is not considered here. Next, by comparing the errors of the basis functions that have high polynomial degree but low regularity with other C^{p-1} basis functions, we find that the regularity has a huge influence on the error. No matter in numerical error or the range of high precision, the performance of high regularity basis function is far better than that of low regularity basis function. This means that in practical applications, it is necessary to maintain high regularity as much as possible while meeting geometric modeling needs. Finally, the properties of the errors between POD and snapshots are very similar to that of the numerical error between POD and exact solution.

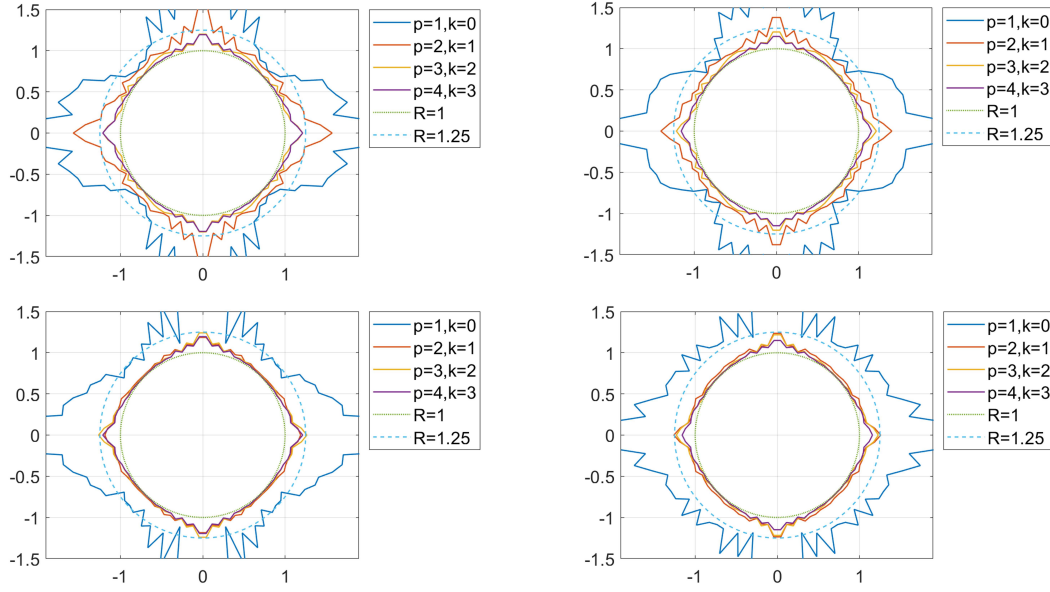


Figure 10: Error figure for compressional wave (left column) and shear wave (right column) using different basis functions with $\nu=0.4$ and $H=0.25$.

3.2 Numerical convergence

We have discussed and analyzed the relationship between the error and the wave vector in detail before. Now we consider numerical convergence of our method. We define the mean numerical error over a time interval between POD solution and exact solution, POD and snapshot as

$$E = \sqrt{\frac{1}{N} \sum_{n=1}^N \|\mathbf{u}_{ex}^n - \mathbf{u}_r^n\|_{L^2}^2} \quad (3.2)$$

and

$$E_r = \sqrt{\frac{1}{N} \sum_{n=1}^N \|\mathbf{u}_s^n - \mathbf{u}_r^n\|_{L^2}^2}, \quad (3.3)$$

where \mathbf{u}_r^n , \mathbf{u}_{ex}^n and \mathbf{u}_s^n are the POD solution, exact solution and snapshot at the n -th time step. Then consider the elastic wave function (2.1) on $\Omega = (0,1.5)^2$ with exact solution:

$$\mathbf{u}(x,y,t) = \frac{1}{1+(x^2+y^2)^{\frac{1}{2}}} \begin{pmatrix} \cos\left(\frac{2\pi\log(t+1)}{(1+x+y)} - 10(x^2+y^2)\right) \\ \sin\left(\frac{2\pi\log(t+1)}{(1+x+y)} - 10(x^2+y^2)\right) \end{pmatrix}. \quad (3.4)$$

We set $\lambda = 0.5769$, $\mu = 0.3846$, $\rho = 1$ and $\zeta = 0$. Consider time interval $[0,1]$ for snapshot, $[0,5]$ for POD and $\Delta t = 10^{-3}$ for both snapshot and POD. We choose $\epsilon_{tol} = 10^{-8}$, and solve

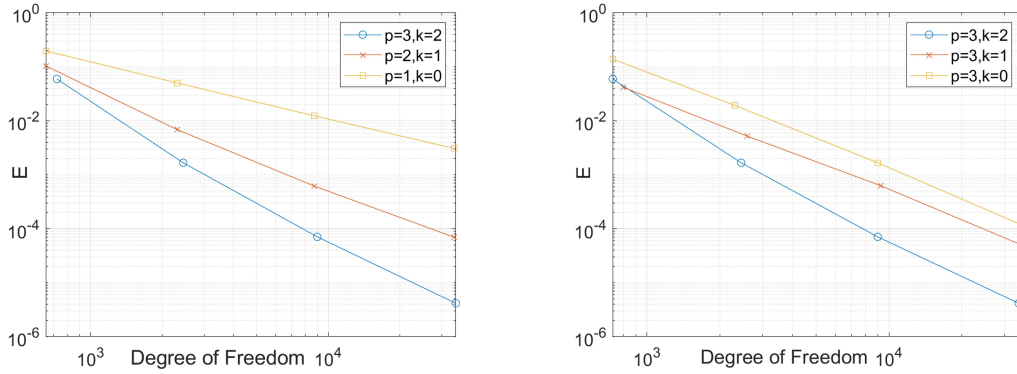


Figure 11: Mean L^2 error between POD ($N_r=16$) and exact solution over time interval $[0,5]$ with respect to degree of freedom.

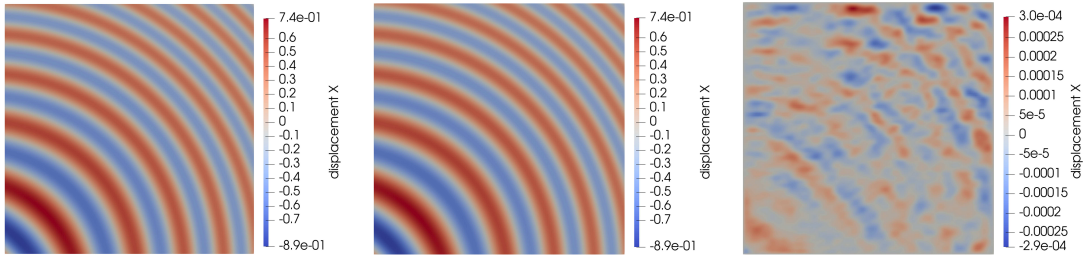


Figure 12: Snapshot, POD solution ($N_r=16$) and their relative difference in x -direction at $t=1$.

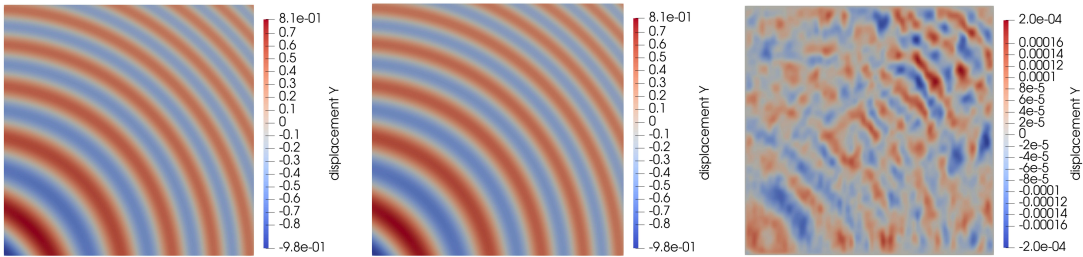


Figure 13: Snapshot, POD solution ($N_r=16$) and their relative difference in y -direction at $t=1$.

the equation several times with different basis functions. Mean L^2 errors between POD and exact solution over time interval $[0,5]$ with respect to total degree of freedom N_{dof} for different basis function group are shown in Fig. 11. Displacements in X and Y directions for snapshot, POD and difference between them at $t=1$ are given in Fig. 12 and Fig. 13. Both figures have reached the expected accuracy and verified the theoretical convergence order of IGA. Then we consider the effect of N_r on error between POD and snapshot. Define truncation of λ as $\Lambda_t = \sum_{i=N_r+1}^N \lambda_i$, and relative error to be $\frac{E}{\|u_{ex}(t=0.5)\|_{L^2}}$. Let N_r take

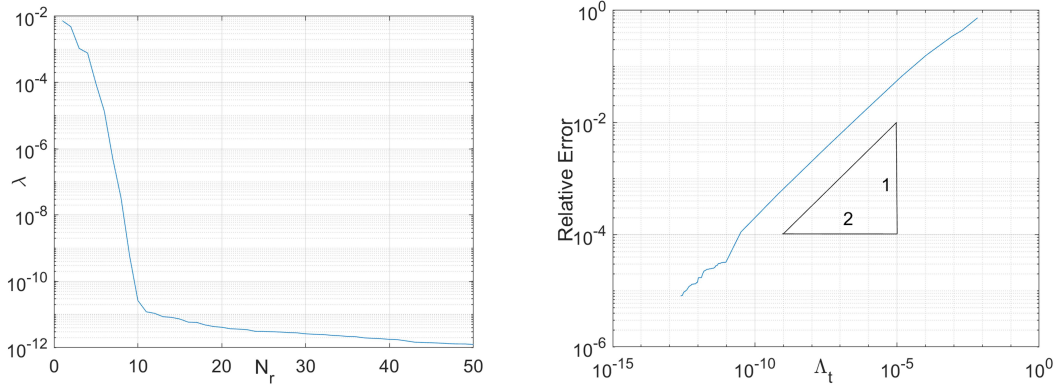


Figure 14: First 50 eigenvalues and the relation between relative error and Δ_t over time interval $[0,5]$.

over 1 to 50. Then the first 50 eigenvalues in (2.27) and relation between relative error and Δ_t are shown in Fig. 14. It can be seen from the figure that a small number of POD modes can control the error within a small range, thereby greatly reducing the scale of the problem. Meanwhile, the square of the relative error is proportional to the truncation error, which means that the error between POD and exact solution can be controlled by ϵ_{tol} . This property is also mentioned in [36].

4 Numerical examples

In the previous section, we have discussed the error property of the IGA-POD method for elastic wave function in detail. Now we consider the propagation of elastic wave in 3D linear elastic media and multipatch physical domain. All of the results are based on GeoPDEs [15] on MATLAB.

4.1 Example 1

We consider evolutions of displacement and stress in a stainless steel spring with a rectangular cross section. The initial control points and a refined mesh are presented in Fig. 15. We choose the $\rho = 7930 \text{ kg/m}^3$, $E = 1.25 \times 10^{11} \text{ Pa}$, $\nu = 0.25$, $\zeta = 6.283 \times 10^{-2}$, $p = 2$, $k = 1$, number of quadrature points in each parametric direction of each element $q = 3$, mesh number each parametric direction $(h_1^{-1}, h_2^{-1}, h_3^{-1}) = (240, 4, 4)$, $N_{\text{dof}} = 21708$, $\epsilon_{\text{tol}} = 10^{-8}$, and $\Delta t = 5 \times 10^{-5}$. POD solution is solved on time interval $[0,1]$, and snapshots are solved on time interval $[0,0.03]$. We assume a impulse displacement alongside y direction $\mathbf{g}_D = (0, \mathbf{g}_{y_D}, 0)^T$, $\mathbf{g}_{y_D} = A(1 - 2I(t - t_0)^2)e^{-I(t - t_0)^2}$, where $A = 10^{-2}$, $I = 10^6$, $t_0 = 7.5 \times 10^{-3}$. \mathbf{g}_D is applied on one square surface $\Gamma_D = \{(x, y, z)^T | z = 0, x \in [0.35, 0.45], y \in [-0.05, 0.05]\}$. Then natural Neumann condition is set on all other surfaces. Evolution of the magnitude of displacement and stress for POD-solution are shown respectively in Fig. 16 and

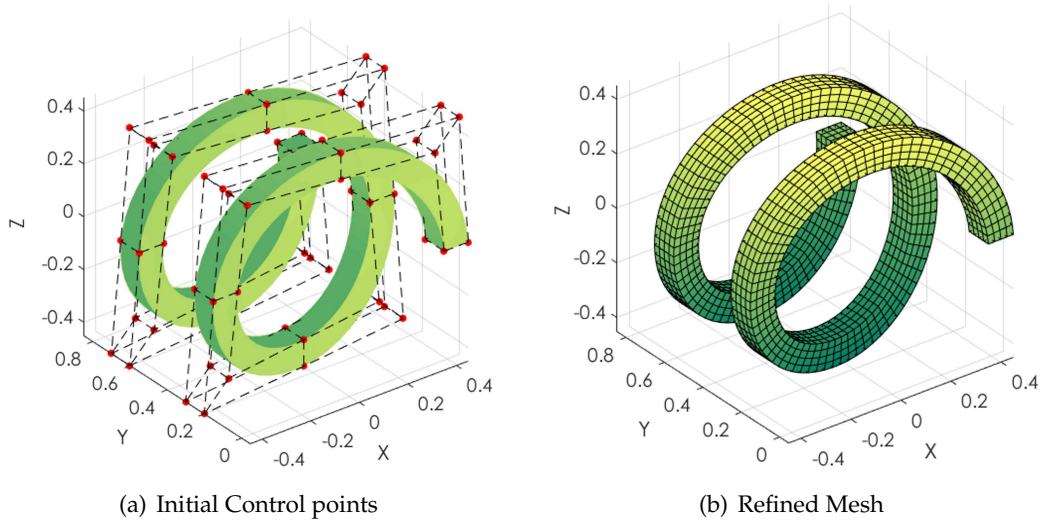


Figure 15: Configurations of Example 1.

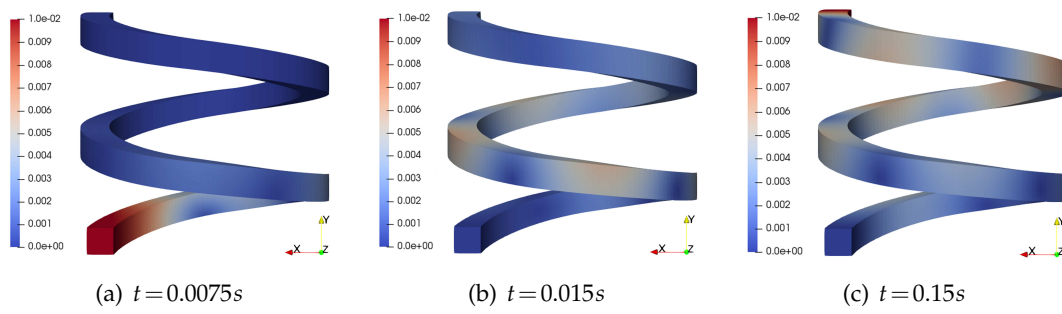


Figure 16: Magnitude of displacement for POD solution with $N_r = 29$ at different time for Example 1.

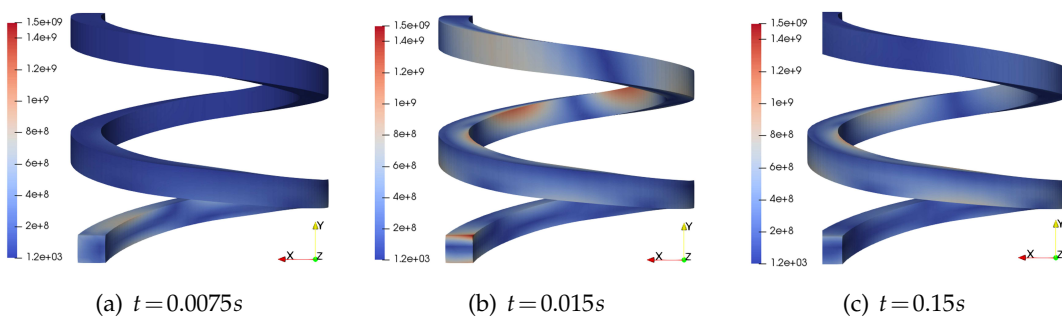


Figure 17: Magnitude of stress for POD solution with $N_r = 29$ at different time for Example 1.

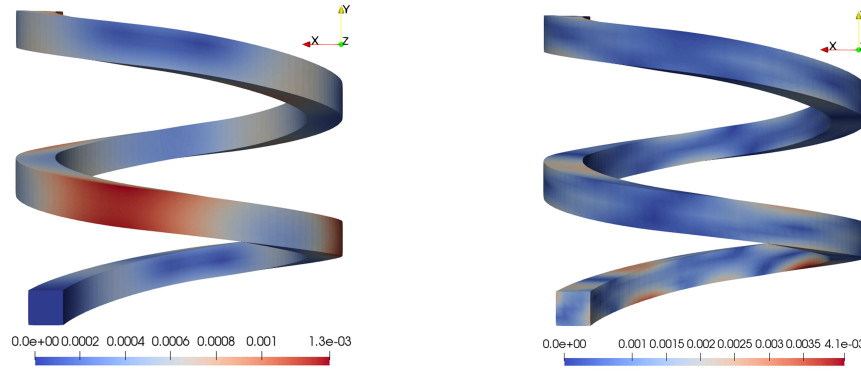


Figure 18: Magnitude of the relative difference in displacement (left) and stress (right) between snapshots and POD solution at $t = 0.015$ for Example 1.

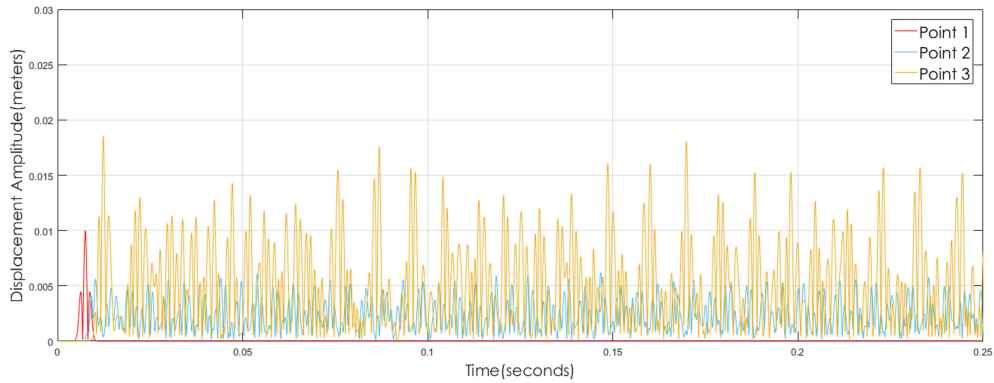


Figure 19: Magnitude of displacement for POD solution with respect to time at different spatial points for Example 1.

Fig. 17. Magnitude of the difference in displacement and stress between POD solution and snapshot are exhibited in Fig. 18. Then we consider a high-fidelity model with the same time step on time interval $[0,1]$ and compare it with the POD method. CPU time for both methods are illustrated in Table 1. We find that, POD reduces much computational costs at the expense of a little accuracy. Finally we consider three points for the POD solution: Point 1, Point 2 and Point 3, whose spatial coordinates at $t = 0$ are $(0.4,0,0)^T$, $(0.4,0.4,0)^T$ and $(0.4,0.8,0)^T$, respectively. The magnitude of displacement over time at these three points are presented in Fig. 19.

4.2 Example 2

Now we consider the wave propagation problem with multi-patch geometry that describes a heterogeneous media. The initial control points, refined mesh and patch configuration are shown in Fig. 20. The computational domain Ω is composed by 4 different

Table 1: CPU time (seconds) for Example 1.

Process	High-fidelity model	Reduced-order model
Assemble data structures and IGA matrices	91	91
High-fidelity solution (Snapshots)	24004	724
POD and POD matrices assembling	/	8
Reduced-order solution	/	3193
Total	24095	4016

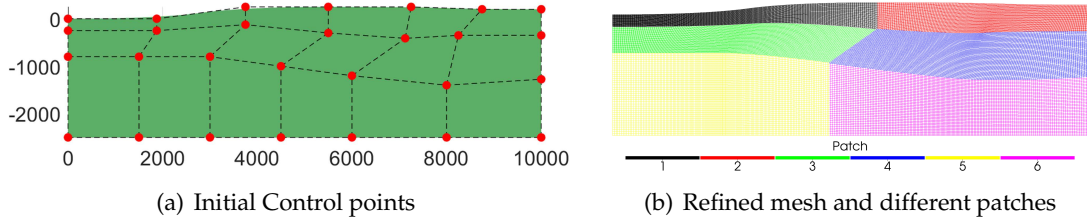


Figure 20: Configurations of Example 2.

materials, their physical parameters can be found in Table 2. We set homogeneous Dirichlet boundary on $\Gamma_D = \{(x,y)^T | x=0 \text{ or } x=10000 \text{ or } y=-2400\}$, natural boundary condition on $\Gamma_N = \partial\Omega/\Gamma_D$, initial displacement $\mathbf{u}_0 = \mathbf{0}$ and initial velocity \mathbf{v}_0 :

$$\mathbf{v}_0 = \begin{cases} (0, -10)^T & \text{if } (x,y)^T \in \Gamma_N \text{ and } x \in [4975, 5025], \\ (0, 0)^T & \text{otherwise.} \end{cases} \quad (4.1)$$

Then let $p = 3$, $k = 2$, number of quadrature points in each parametric direction of each element $q = 3$, number of mesh subdivision in each patch $(\hat{h}_1^{-1}, \hat{h}_2^{-1}) = (320, 40)$, $N_{dofs} = 164338$, $\epsilon_{tol} = 10^{-8}$ and $\Delta t = 5 \times 10^{-3}$. POD solution is solved on time interval $[0, 2]$, and snapshots are solved on time interval $[0, 0.5]$. Magnitude of displacement and stress for POD solution at different time are shown in Fig. 21, from these figures we can clearly see how the wave travel through the media, reflect and refract at boundaries between different media. Notice that the boundaries between different media are marked with white curves. The magnitude of the relative differences in displacement and stress at $t = 1$ between snapshot of a high-fidelity model and POD solution are shown in Fig. 22, as we can see for both displacement and stress, IGA-POD yields a good result. Then, we consider a point $(4002, 221)^T$ at top boundary. Horizontal and vertical displacements at the point from POD solution over time interval $[0, 2]$ are illustrated in Fig. 23. Finally, the CPU time is compared to a high-fidelity model which is solved on time interval $[0, 2]$. The results are shown in Table 3.

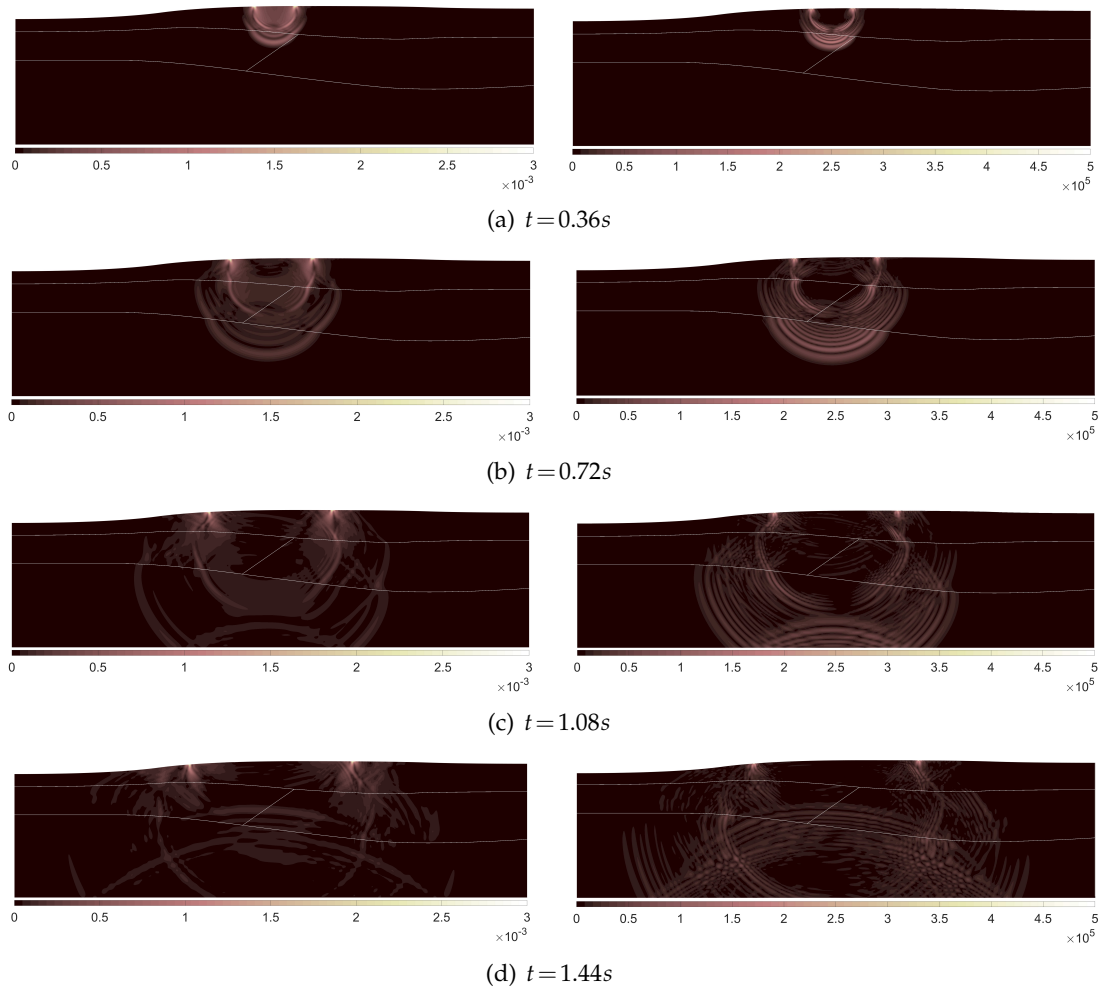


Figure 21: Magnitude of displacement (left) and stress (right) for POD solution with $N_r = 187$ at different times for Example 2.

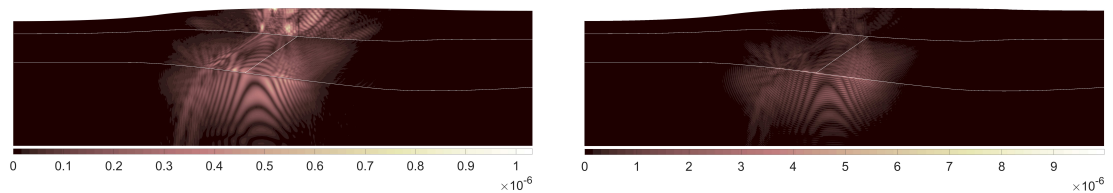


Figure 22: Magnitude of the relative difference in displacement (left) and stress (right) between snapshots and POD solution at $t = 1$ for Example 2.

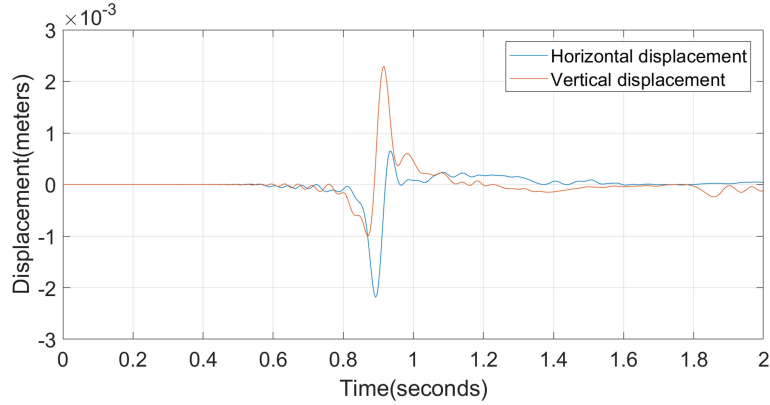


Figure 23: Horizontal and vertical displacement for POD solution with respect to time at $(4002, 221)^T$ for Example 2.

Table 2: Material configuration for Example 2.

Material ID	Range	$\rho [kg/m^3]$	$\zeta [s^{-1}]$	$E [pa]$	ν
1	On patch 1 and 2	1800	0.0680	6.12×10^9	0.025
2	On patch 3	1800	0.0444	1.44×10^{10}	0.025
3	On patch 4	2050	0.0308	1.54×10^{10}	0.053
4	On patch 5 and 6	2450	0.0125	3.80×10^{10}	0.125

Table 3: CPU time (seconds) for Example 2.

Process	High-fidelity model	Reduced-order model
Assemble data structures and IGA matrices	843	843
High-fidelity solution (Snapshots)	2515	630
POD decomposition and POD matrices assembling	/	136
Reduced-order solution	/	477
Total	3358	2085

5 Conclusions

We have presented the POD method combined with IGA and the generalized- α method for elastodynamics. Numerical dispersion and numerical convergence are investigated in detail through various numerical examples. In summary, the IGA-POD method can be effectively applied to elastic wave problems with high accuracy and efficiency. It reduces computational costs without losing too much accuracy, while exhibiting good properties in numerical dispersion. The advantages of convenient geometric modeling for different

domains including multi-patch circumstances and exact geometry representations have been shown in numerical examples. Another interesting aspect is that the time interval for snapshots and the time interval for POD are not necessarily the same. This means that a snapshots computed in advance can usually be applied outside their original time interval. However, time interval for snapshots cannot be too small. Otherwise the physical information of the elastic wave will not be captured correctly, which results in spurious solution with huge numerical error.

Acknowledgments

This work is supported by the National Natural Science Foundation of China (Grant nos. 11771393, 11632015, 12071149), Natural Science Foundation of Zhejiang Province (Grant no. LZ14A010002), National Science Foundation of Shanghai (Grant no. 19ZR1414100), Science and Technology Commission of Shanghai Municipality (No. 18dz2271000) and the Fundamental Research Funds for the Central Universities.

References

- [1] P.B. Silva, A.L. Goldstein, and J.R.F. Arruda, Building spectral element dynamic matrices using finite element models of waveguide slices and elastodynamic equations, *Shock and Vibration*, 20.3(2013) 439-458.
- [2] H. Singh, J. Shragge, and I. Tsvankin, Coupled-domain acoustic-elastic solver for anisotropic media: A mimetic finite difference approach, *SEG Technical Program Expanded Abstracts 2019*, 3755-3759.
- [3] A. Quarteroni, A. Manzoni, and F. Negri, *Reduced Basis Methods for Partial Differential Equations*, Springer, 2016.
- [4] G. Berkooz, P. Holmes, and J.L. Lumley, The proper orthogonal decomposition in the analysis of turbulent flows, *Ann. Rev. Fluid. Mech.* 25 (1993) 539-575.
- [5] K. Kunisch and S. Volkwein, Galerkin proper orthogonal decomposition methods for parabolic problems, *Numer. Math.* 90 (2001) 117-148.
- [6] T. Iliescu and Z. Wang, Variational multiscale proper orthogonal decomposition: Convection-dominated convection-diffusion-reaction equations, *Math. Comput.* 82 (2013) 1357-1378.
- [7] J.R. Singler, New POD error expressions, error bounds, and asymptotic results for reduced order models of parabolic PDEs, *SIAM J. Numer. Anal.* 52 (2014) 852876.
- [8] S. Zhu, L. Dedè, and A. Quarteroni, Isogeometric analysis and proper orthogonal decomposition for parabolic problems, *Numer. Math.* 135 (2017) 1-38.
- [9] S. Zhu, L. Dedè, and A. Quarteroni, Isogeometric analysis and proper orthogonal decomposition for the acoustic wave equation, *ESAIM Math. Model. Numer. Anal.* 51 (2017) 1197-1121.
- [10] Y. Bazilevs, J.A. Cottrell, T.J.R. Hughes, and G. Sangalli, Isogeometric analysis: Approximation, stability and error estimates for h -refined meshes, *Math. Models Methods Appl. Sci.* 16 (2006) 1031-1090.

- [11] A. Buffa, G. Sangalli, and R. Vázquez, Isogeometric analysis in electromagnetics: B-splines approximation, *Comput. Methods Appl. Mech. Engrg.* 199 (2010) 1143-1152.
- [12] J. Cottrell, T.J.R. Hughes, and Y. Bazilevs, *Isogeometric Analysis: Toward Integration of CAD and FEA*, Wiley Publishing, 2009.
- [13] T.J.R. Hughes, J. Cottrell, and Y. Bazilevs, Isogeometric analysis: CAD, finite elements, NURBS, exact geometry and mesh refinement, *Comput. Methods Appl. Mech. Engrg.* 194 (2005) 4135-4195.
- [14] L. Piegl and W. Tiller, *The NURBS Book*, Springer Berlin Heidelberg, 1997.
- [15] C. de Falco, A. Reali, and R. Vázquez, GeoPDEs: A research tool for isogeometric analysis of PDEs, *Adv. Engrg. Softw.* 42 (2011) 1020-1034.
- [16] J. Chung and G.M. Hulbert, A time integration algorithm for structural dynamics with improved numerical dissipation: The Generalized- α Method, *J. Appl. Mech.* 60 (1993) 371-375.
- [17] R. Stacey, Improved transparent boundary formulations for the elastic-wave equation, *Bull. Seismol. Soc. Am* 78 (1988) 2089-2097.
- [18] P.F. Antonietti, I. Mazzieri, A. Quarteroni, and F. Rapetti, Non-conforming high order approximations of the elastodynamics equation, *Comput. Methods Appl. Mech. Engrg.* 209-212 (2012) 212-238.
- [19] E.J. Kenneth, C.H. Whiting, and G.M. Hulbert, A generalized- α method for integrating the filtered Navier-Stokes equations with a stabilized finite element method, *Comput. Methods Appl. Mech. Engrg.* 190 (2000) 305-319.
- [20] L. Dedè, C. Jäggli, and A. Quarteroni, Isogeometric numerical dispersion analysis for two-dimensional elastic wave propagation, *Comput. Methods Appl. Mech. Engrg.* 284 (2015) 320-348.
- [21] G. Seriani and S.P. Oliveira, Dispersion analysis of spectral element methods for elastic wave propagation, *Wave Motion* 45 (2008) 729-744.
- [22] J.D.D. Basabe and M.K. Sen, Stability of the high-order finite elements for acoustic or elastic wave propagation with high-order time stepping, *Geophys. J. Roy. Astr. S.* 181 (2010) 577-590.
- [23] J. Diaz and M.J. Grote, Energy conserving explicit local time stepping for second-order wave equations, *SIAM J. Sci. Comput.* 31 (2009) 1985-2014.
- [24] J.M. Carcione, Elastodynamics of a non-ideal interface: Application to crack and fracture scattering, *Geophys. J. Roy. Astr. S.* 1012 (1996) 28177-28188.
- [25] U. Basu and A.K. Chopra, Perfectly matched layers for time-harmonic elastodynamics of unbounded domains: Theory and finite-element implementation, *Comput. Methods Appl. Mech. Engrg.* 192 (2003) 1337-1375.
- [26] E. Chaljub, Y. Capdeville, and J.P. Vilotte, Solving elastodynamics in a fluid-solid heterogeneous sphere: A parallel spectral element approximation on non-conforming grids, *J. Comput. Phys.* 187 (2003) 457-491.
- [27] M. Ainsworth, Discrete dispersion relation for hp-version finite element approximation at high wave number, *SIAM J. Numer. Anal.* 42 (2005) 553-575.
- [28] L.L. Thompson, A review of finite-element methods for time-harmonic acoustics, *J. Acoust. Soc. Am.* 119 (2006).
- [29] I. Mazzieri and F. Rapetti, Dispersion analysis of triangle-based spectral element methods for elastic wave propagation, *Numer. Algo.* 60 (2012) 631-650.
- [30] G. Seriani and S.P. Oliveira, Dispersion analysis of spectral element methods for elastic wave propagation, *Wave Motion* 45 (2008) 729-744.
- [31] F. Casadei, E. Gabellini, G. Fotia, F. Magglio, and A. Quarteroni, A mortar spectral/finite

- element method for complex 2D and 3D elastodynamic problems, *Comput. Methods Appl. Mech. Engrg.* 191 (2002) 5119-5148.
- [32] P. Hauret and P.L. Tallec, A discontinuous stabilized mortar method for general 3D elastic problems, *Comput. Methods Appl. Mech. Engrg.* 196 (2007) 4881-4900.
- [33] E.T. Chung and B. Engquist, Optimal discontinuous Galerkin methods for wave propagation, *SIAM J. Numer. Anal.* 44 (2006) 2131-2158.
- [34] M.J. Grote, A. Schneebeli, and D. Schötzau, Discontinuous Galerkin finite element method for the wave equation, *SIAM J. Numer. Anal.* 44 (2006) 2408-2431.
- [35] T.J.R. Hughes, A. Reali, and G. Sangalli, Duality and unified analysis of discrete approximations in structural dynamics and wave propagation: Comparison of p -method finite elements with k -method NURBS, *Comput. Methods Appl. Mech. Engrg.* 197 (2008) 4104-4124.
- [36] R. Li, Q. Wu, and S. Zhu, Proper orthogonal decomposition with SUPG-stabilized isogeometric analysis for reduced order modelling of unsteady convection-dominated convection-diffusion-reaction problems, *J. Comput. Phys.* 387 (2019) 280-302.
- [37] E. Zampieri and L.F. Pavarino, Explicit second order isogeometric discretizations for acoustic wave problems, *Comput. Methods Appl. Mech. Engrg.* 348 (2019) 776-795.
- [38] A. Quarteroni, A. Tagliani, and E. Zampieri, Generalized Galerkin approximations of elastic waves with absorbing boundary conditions, *Comput. Methods Appl. Mech. Engrg.* 163 (1998) 323-341.
- [39] S. Volkwein and K. Kunischs, Galerkin proper orthogonal decomposition methods for general equation in fluid dynamics, *SIAM J. Numer. Anal.* 40.2 (2003) 492-515.
- [40] S. Perotto, A. Reali, P. Rusconi, and A. Veneziani, HIGAMod: A hierarchical isogeometric approach for model reduction in curved pipes, *Comput. & Fluids* 142 (2016) 21-29.
- [41] L. Chamoin and H.P. Thai, Certified real-time shape optimization using isogeometric analysis, PGD model reduction, and a posteriori error estimation, *Internat. J. Numer. Methods Engrg.* 119.3 (2019) 151-176.
- [42] S. Georgaka, G. Stabile, G. Rozza, and M.J. Bluck, Parametric POD-Galerkin model order reduction for unsteady-state heat transfer problems, *Commun. Comput. Phys.* 27 (2020) 1-32.